



Deep-seated thrust faults bound the Mare Crisium lunar mascon



Paul K. Byrne^{a,b,*}, Christian Klimczak^{b,c}, Patrick J. McGovern^a, Erwan Mazarico^d, Peter B. James^e, Gregory A. Neumann^d, Maria T. Zuber^f, Sean C. Solomon^{b,e}

^a Lunar and Planetary Institute, Universities Space Research Association, Houston, TX 77058, USA

^b Department of Terrestrial Magnetism, Carnegie Institution of Washington, Washington, DC 20015, USA

^c Department of Geology, University of Georgia, Athens, GA 30602, USA

^d Solar System Exploration Division, NASA Goddard Space Flight Center, Greenbelt, MD 20771, USA

^e Lamont–Doherty Earth Observatory, Columbia University, Palisades, NY 10964, USA

^f Department of Earth, Atmospheric and Planetary Sciences, Massachusetts Institute of Technology, Cambridge, MA 02139, USA

ARTICLE INFO

Article history:

Received 15 November 2014

Received in revised form 31 May 2015

Accepted 13 June 2015

Available online xxxx

Editor: C. Sotin

Keywords:

GRAIL

LRO

Mare Crisium

mascon

Moon

thrust faults

ABSTRACT

Mare Crisium is composed of a set of volcanic deposits situated in an impact basin on the Moon's near side. The topography of the mare is dominated by an annulus of elevated topography, the inner edge of which is delineated by basin-concentric wrinkle ridges. From a combination of remotely sensed image and topographic data and numerical modeling, we show that the thrust faults that underlie these ridges penetrate up to 20 km in depth, considerably below the base of the mare deposits themselves. Thrust faults of this scale have not heretofore been recognized on the Moon. Mare Crisium sits above a region of uplifted mantle, which contributes to a mass excess beneath the basin, and we demonstrate by comparison with free-air gravity anomaly and derived crustal thickness data for Crisium that the thrust faults structurally bound this elevated mantle material. By means of finite-element models of stresses induced by lithospheric loading within the basin, we argue that the deep-seated thrusts may have been localized by the boundary between the superisostatic mantle material and a sub-isostatic collar of thickened crust that resulted from basin formation and modification shortly after impact. Importantly, numerous other mare-filled mascon basins on the Moon share the same topographic and tectonic characteristics as Crisium, suggesting that they, too, are underlain by deep-seated thrust faults that formed in a similar manner.

© 2015 Elsevier B.V. All rights reserved.

1. Introduction

The Moon hosts numerous large impact basins that are filled with volcanic deposits, the lunar maria. Each of these mare deposits shows evidence of post-emplacement tectonic deformation (Bryan, 1973), dominantly in the form of wrinkle ridges, landforms that are interpreted as folds over reverse or thrust faults that may be blind or surface breaking. These ridges have been ascribed to subsidence of the mare deposits (Maxwell et al., 1975), which likely occurred throughout their emplacement (Solomon and Head, 1980). Moreover, a substantial number of lunar maria are associated with positive gravity anomalies termed mass concentrations or “mascons” (Muller and Sjogren, 1968), thought to be the result of some combination of mare loading within, and an elevated, su-

perisostatic crust–mantle boundary beneath, these basins (Zuber et al., 2013a).

Recent combined hydrocode and finite-element modeling has enhanced our understanding of the formation of lunar mascons. Melosh et al. (2013) and Freed et al. (2014) showed that the free-air gravity anomaly pattern that characterizes a lunar mascon results from impact excavation, crater collapse, and the subsequent slow isostatic adjustment of the resultant basin. These and similar models cannot simulate discrete deformation, however, and so do not predict or incorporate the tectonic deformation widely observed in lunar mascon basins. The recent acquisition of high-resolution imaging, topographic, and gravity field data for the Moon by the Lunar Reconnaissance Orbiter (LRO) (Chin et al., 2007) and the Gravity Recovery and Interior Laboratory (GRAIL) (Zuber et al., 2013b) missions presents an opportunity to investigate anew the relationship between subsurface crust–mantle structure and the surficial expression of tectonic deformation within lunar mascon basins.

* Corresponding author at: Lunar and Planetary Institute, Universities Space Research Association, Houston, TX 77058, USA. Tel.: +1 281 486 2140.

E-mail address: byrne@lpi.usra.edu (P.K. Byrne).

In this study, we focus in detail on the tectonic record within, and the mascon beneath, the well-characterized Mare Crisium, situated within the inner ring of a Nectarian-aged impact basin on the Moon's nearside. The central mare deposit is 556 km in east–west and 455 km in north–south extent and hosts basalts emplaced between 3.61 and 2.71 Ga (Hiesinger et al., 2011). First, we use image and topographic data from LRO to remap the tectonic landforms within Crisium. We then estimate the depths of penetration of faults beneath selected prominent wrinkle ridges within the basin with the COULOMB elastic dislocation software. Next, with free-air gravity anomaly data returned by GRAIL, we compare in plan view and in cross-section the geometry of these faults with the elevated mantle material beneath Crisium. Finally, we perform a series of simulations with the TEKTON finite-element code to investigate the means by which such faults might have formed. Because of the occurrence of sets of arcuate wrinkle ridges in other maria associated with free-air gravity anomalies, our results are likely applicable to other lunar mascon basins. Moreover, as mascons have also been reported on Mars (Smith et al., 1993) and Mercury (Smith et al., 2012), these findings may give fresh insight into the formation and evolution of mascons on terrestrial worlds in general.

2. Mapping tectonic features

We surveyed the tectonic landforms of Crisium by combining the global morphologic base map from the Lunar Reconnaissance Orbiter Camera (LROC) wide-angle camera (WAC) (Speyerer et al., 2011) with the LROC WAC-derived digital terrain model (DTM) (Scholten et al., 2012), at effective resolutions of 100 m/pixel and 300 m/pixel, respectively. We augmented our mapping effort with DTM-derived artificially illuminated hillshade maps generated with lighting angles of 0° and 180° azimuth (measured clockwise from north) compared with 90° and 270° azimuth from solar illumination alone. These map products aided in the identification of east–west-oriented structures that might not be readily visible in photogeological data alone because of unfavorable lighting conditions.

Consistent with previous observations (e.g., Solomon and Head, 1980), we find that the basin interior is replete with wrinkle ridges, manifest as broad, low-relief arches with scarp-like sides. Numerous examples are superposed by narrow, crenulated ridges, which may overlie small backthrusts (Schultz, 2000; Mueller and Golombek, 2004). In our survey, we documented more than 170 ridges (Fig. 1a). These landforms are located throughout the mare interior, and many show no strongly preferred orientations. The most prominent wrinkle ridges, however, parallel the mare outline and verge (i.e., show evidence for horizontal displacement) toward the interior, most notably at azimuths of 30°–180° and 260°–330°. At ~90° azimuth, a large ridge deviates from this pattern and strikes ~east–west. When compared with topographic data for the mare, those prominent concentric ridges appear to define the inner boundary of the elevated annular “bench” within Crisium reported by Zisk et al. (1978) (Fig. 1b). The difference in elevation between the bench and the mare interior is as much as 500 m (e.g., at Dorsum Oppel and Dorsa Tetyaev).

Subtle, ridge-like changes in relief across the mare are revealed by the DTM data but are virtually impossible to detect otherwise. Notable examples are found in the western portion of the basin interior, trending ~north–south (Fig. 1a). We term these 13 landforms, 30–100 km in length, “broad ridges.” Although their origin is unknown, they may represent additional shortening structures that have no surficial faulted component. Alternatively, these ridges may be an earlier set of wrinkle ridges formed at some point prior to the last phase of mare emplacement (cf. Head et al., 1978), their

topographic signature subsequently tempered by the deposition of later lavas.

Imaging data show 10 craters within Crisium that have been partially buried by mare deposits. Our tectonic map hints at a further five that are demarcated by wrinkle ridges but have no other surface manifestation (Fig. 1a). The largest such example is 91 km in diameter. Under the assumption that this landform is a crater, its ratio of rim height to rim-crest diameter implies a minimum fill depth of ~1.4 km (Eq. (4) of Pike, 1977). This value represents, by extension, a minimum value for mare thickness within Crisium. Earlier estimates of 3.5–4 km have been given for the maximum cumulative mare thickness in the basin (Zisk et al., 1978; Mullis, 1992), implying that this large crater lies substantially below the present mare surface (and accounting for why it is resolvable only with topographic data).

3. Modeling the maximum depth of faulting

To determine the geometries of the faults that bound the inner edge of the bench within Crisium, we took profiles from the Lunar Orbiter Laser Altimeter (LOLA) gridded DTM (118 m/pixel) (Smith et al., 2010) across four prominent concentric ridges, Dorsa Terrier, Oppel, Tetyaev, and Harker, and the unnamed eastern ridge (profiles a–e in Fig. 1b). We also investigated a smaller ridge in the basin interior (profile f in Fig. 1b), for comparison with the larger bench-bounding structures. With the open-access elastic dislocation program COULOMB (Lin and Stein, 2004), we then matched model solutions for surface displacements to the topographic profiles (Fig. 2a–f).

Given the stress functions for an elastic half-space (Okada, 1992), parameters such as dip angle, burial and penetration depths, and the direction and amount of displacement can be varied individually for a model fault until a satisfactory match to LOLA topography is found. Once such a match is obtained, we may assume that the parameters of the model fault are a good approximation to the corresponding parameters of the fault under consideration (Schultz et al., 2010) (Table 1). This approach is particularly suited to the Moon because, with virtually no erosion, present-day topographic relief across a fault-related landform may be equated to the surface displacement produced by the underlying structure (absent any burial by volcanic material of part or all of the surrounding surface). The dimensions of a given wrinkle ridge inform its initial parameterization. For example, the combination of fault dip angle and depth of faulting specifies the width or down-dip extent of a fault, and fault displacement controls the structural relief of the associated landform. We varied the fault dip angle by increments of 2° from a starting dip angle of 30°, reducing the increment size to 1° when finalizing a model fit. The depth of faulting was altered in 1-km steps. The fault displacement did not require substantial variation because this parameter is related to ridge height for a given fault dip angle, and so it was adjusted by increments of 10 m (and even 5 m for the smaller ridges) until matched to the measured profile. Importantly, we tapered the fault displacement with increasing depth, even for a ridge for which the underlying fault was homoclinal (i.e., constant dip angle), to represent the likely spatial variation of displacement along a fault (e.g., Pollard and Segall, 1987). Neglecting this tapering results in unphysical edge effects in the models and would yield a highly unusual scenario for lithospheric-scale faults. It was through this process that we discovered that some ridges had morphologies that could not be matched with homoclinal fault planes but instead required listric (i.e., curved) fault geometries (approximated by as few as two or as many as nine segments linear in cross section and of differing dip).

To characterize the goodness of fit of our models, we calculated the root mean squared (RMS) error of each model profile.

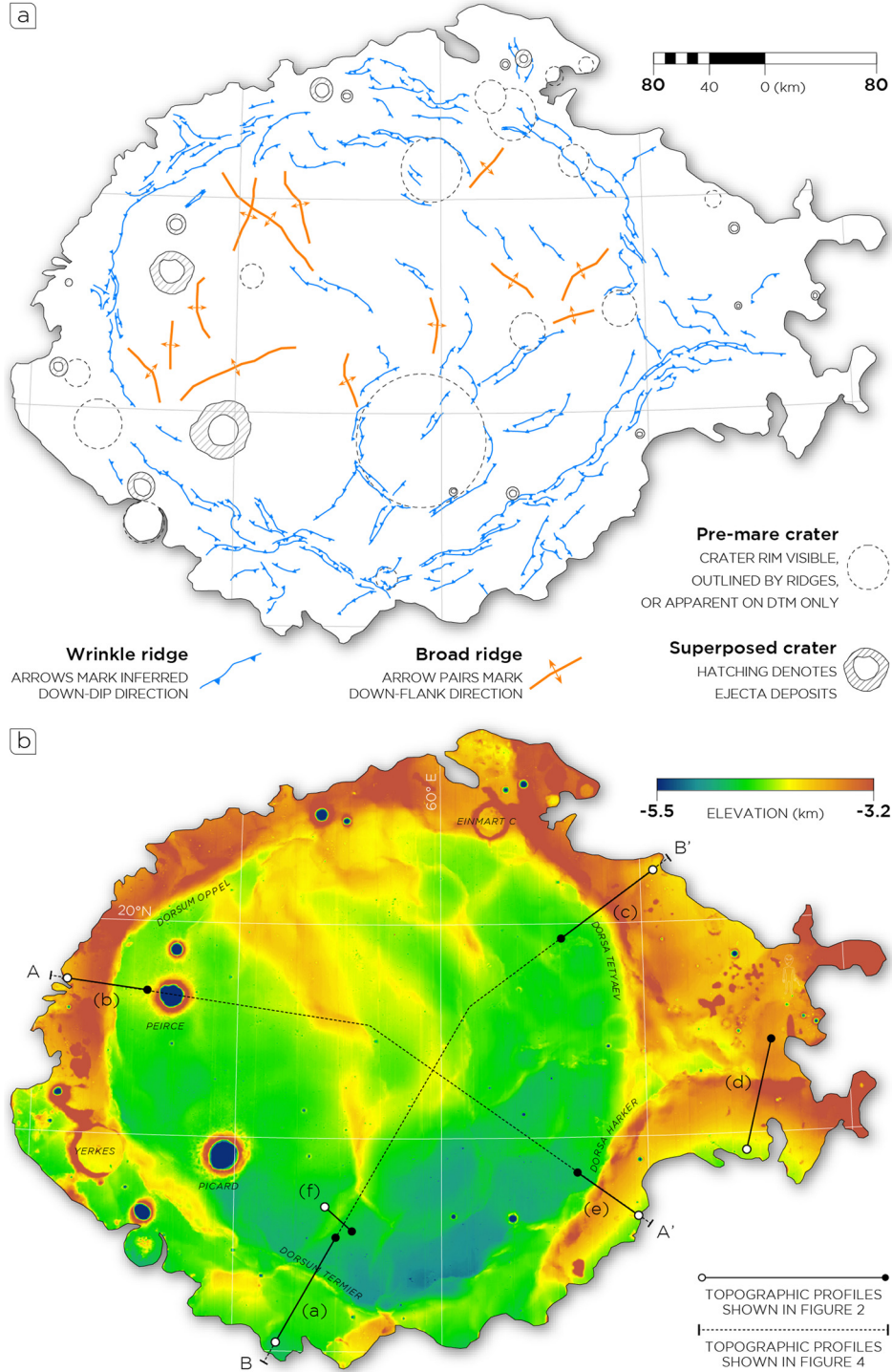


Fig. 1. Tectonic landforms and physiography of Mare Crisium. **(a)** Structural map of the basin interior. **(b)** Color-coded elevation map of the mare deposits. Topographic data from the 100 m/pixel LROC WAC DTM. Solid and dashed black lines correspond to topographic profiles shown in Figs. 2 and 4, respectively. Prominent physiographic features are labeled. Maps are in orthographic projection, centered at 17.1°N, 59.4°E.

We first interpolated the model sampling frequency in horizontal distance to match that of the measured profiles, and we then set the lengths of the model profiles to those of the corresponding measured profiles. This approach ensured that the relevant portion of each model profile could be compared in a straightforward manner with measured data. The RMS errors of the model profiles, also given in Table 1, are in each case on the order of tens of meters, with the most accurate fits for profiles (a) and (f). Notably, for those cases with the largest RMS errors, e.g., profiles (c) to (e),

the topographic profiles may reflect surface modification by processes other than faulting that are not included in the model. For example, there is a substantial difference between our model solution and measured topography for profile (d) at the base of the structure (Fig. 2d), which may be the result of constructional (i.e., volcanic) processes. Upon removal of that portion of the profile from our goodness-of-fit analysis, the RMS error for profile (d) falls from 43.7 m to 14.1 m. Similarly, profile (e) features a sharp increase in elevation at its southern end (Fig. 2e), which corresponds

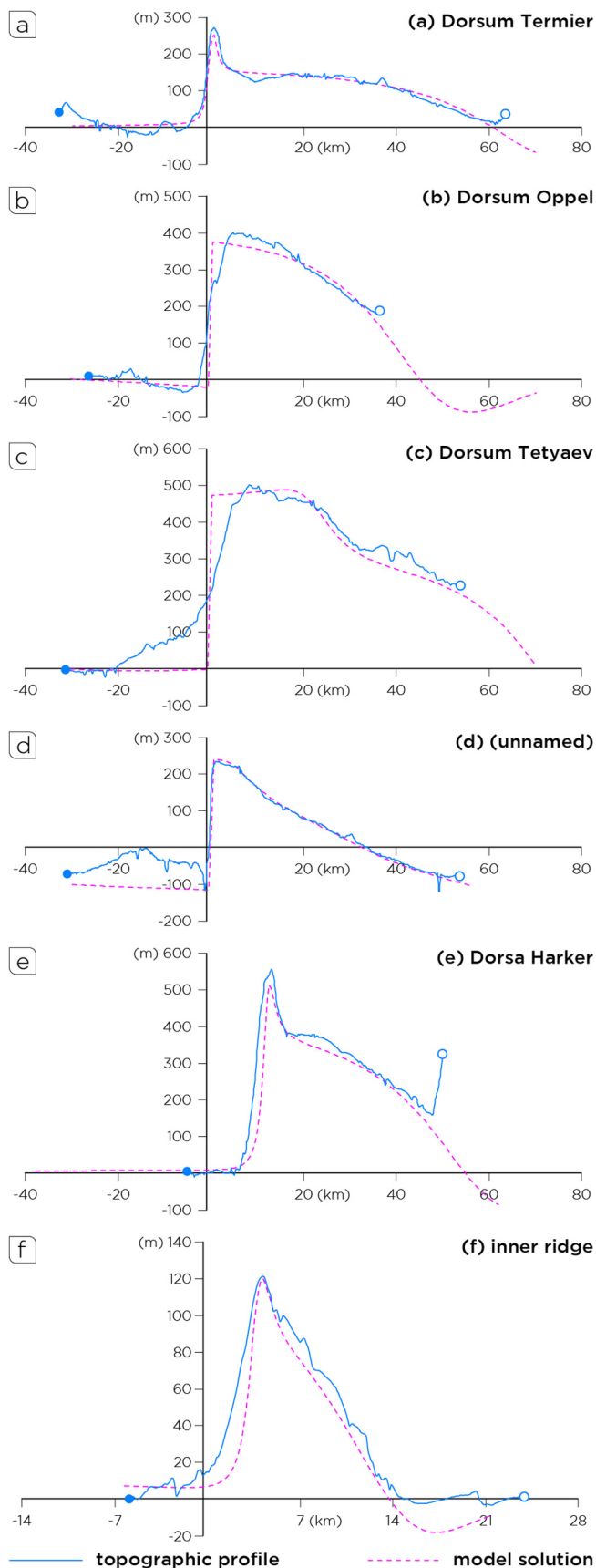


Fig. 2. Topographic profiles (blue) and modeled surface displacements (pink) for wrinkle ridges along the interior edge of the annular “bench” within Crisium (a–e) and for an exemplar ridge near the basin center (f). Profiles (a–e) are shown with a vertical exaggeration of 80:1; profile (f) has a vertical exaggeration of 136:1.

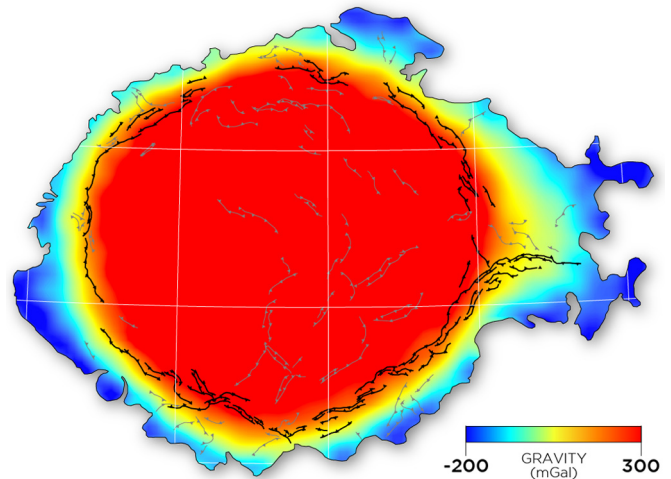


Fig. 3. GRAIL free-air gravity anomaly map (to degree and order 320) for the interior of Mare Crisium. Gravity anomalies are given in mGal. The surface traces of wrinkle ridges along the interior of the annular “bench” are shown in black; all other mapped wrinkle ridges are shown in grey. Map symbology and projection are as those in Fig. 1.

to the perimeter of the interior basin wall (Fig. 1b). Excluding this portion of the profile from our calculation yields an RMS error of 51.6 m rather than 59.4 m (a reduction of 13%). Impact craters also contribute to short-wavelength deviations between model and topographic profiles, but their effect is minor.

We find that the faults beneath the five prominent bench ridges accumulated substantial dip-slip displacements (550–1600 m; see Table 1). Moreover, despite differences in fault geometry (the modeled faults underlying Dorsa Tetyaev and the unnamed eastern ridge are listric, whereas those below Dorsa Termier, Oppel, and Harker are planar) all five structures penetrate ~18–20 km into the lunar lithosphere, far below the base of the mare deposits. The ridge interior to the bench also overlies a listric fault, although the ridge has substantially less relief (Fig. 2f) and the associated fault penetrates only 6 km below the mare surface. We note, nonetheless, that this depth is also below the likely base of the mare–basement interface (Zisk et al., 1978). In all cases, the range of dip angles of these faults is 5–25° (Table 1), lower than values of the optimal angle for frictional sliding of a typical basalt, as commonly adopted in fault analyses (e.g., Byrne et al., 2014).

4. Gravity data

We used GRAIL free-air gravity anomaly data (from a spherical harmonic expansion to degree and order 320, equivalent to a spatial block size of 17 km) from the Mare Crisium region. With these data, we compared the spatial extent and cross-sectional profile of the Crisium mascon with the areal distribution and subsurface geometry of the faults beneath the prominent concentric ridges inside the basin.

In plan view, the free-air gravity anomaly signature of the mascon occupies almost the entire mare footprint, with anomalies of ~200 mGal ($1 \text{ mGal} = 10^{-5} \text{ m/s}^2$) at the perimeter, rising to ~300 mGal inward of 0.7–0.8 of the mare radius (Fig. 3). Interestingly, and as noted by Zuber and James (2013), the concentric ridges that follow the inner edge of the topographic bench within Crisium are spatially coincident with the outer boundary of the highest free-air gravity anomaly values (Fig. 3). (This collocation does not apply to the prominent east–west-striking ridge in the eastern portion of the mare.)

To determine how the deep-seated faulting in Mare Crisium relates to the underlying uplifted mantle in cross section, we cal-

Table 1

COULOMB-derived values and RMS misfits for the six wrinkle-ridge faults modeled in this study.

Structure name	Fault type	Displacement (m)	Dip (°)	Burial depth (km)	Penetration depth (km)	RMS misfit (m)
(a) Dorsum Termier	Planar	550	15	1	20	15.7
(b) Dorsum Oppel	Planar	1050	22.5	0	20	32.9
(c) Dorsa Tetyaev	Listric	1600	20 → 11 ^a	0	20	60.9
(d) (unnamed)	Listric	850	25 → 5	0	18	43.7
(e) Dorsa Harker	Planar	1000	22	1.5	20.5	59.4
(f) Inner ridge	Listric	230	25 → 21	1	6	22.9

^a The → symbol indicates that the dip angle of the fault decreases with depth. For these models, this change in dip angle was approximated by at least two contiguous fault planes.

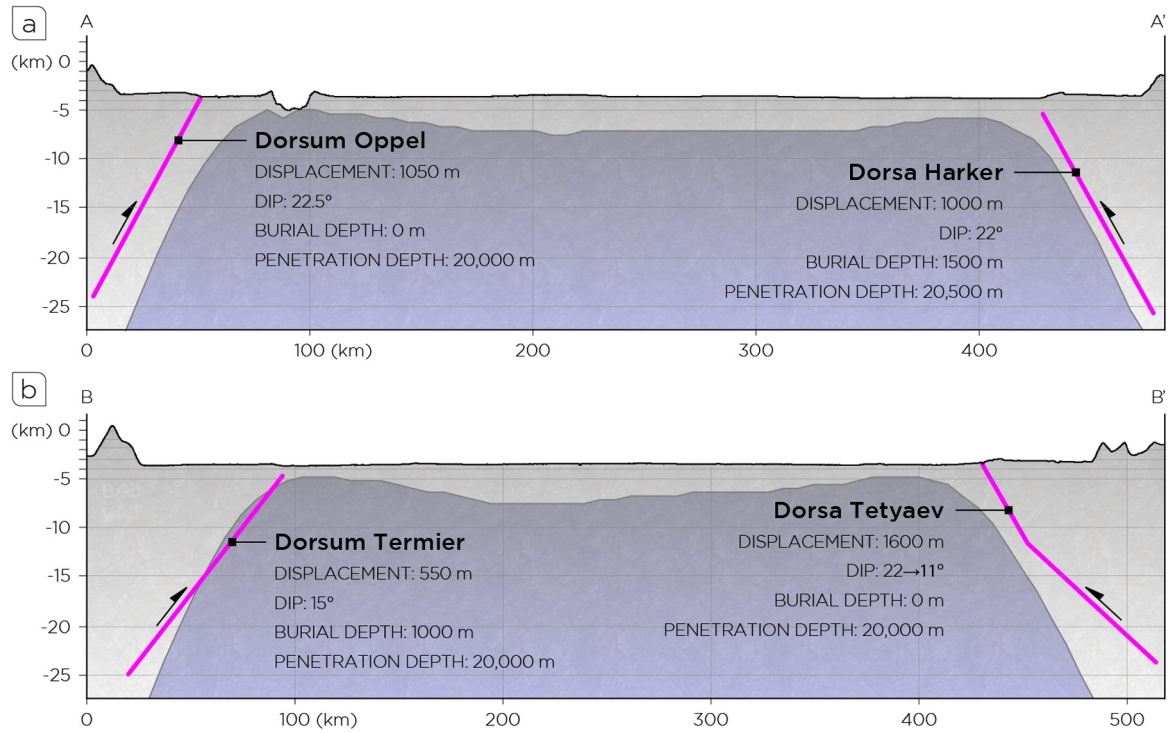


Fig. 4. The subsurface structure of Mare Crisium. (a, b) Cross sections along the topographic profiles A–A' and B–B', respectively, shown in Fig. 1, including surface topography (black line), crust (grey fill), mantle (purple fill), and thrust faults (pink lines), for which geometric properties are given. The cross sections in (a) and (b) are shown with vertical exaggerations of 4.5:1 and 4.8:1, respectively.

culated the depth to the crust–mantle boundary beneath the basin. From the LOLA DTM we subtracted the crustal thickness model of Wiczeorek et al. (2013). This model was obtained from the GRAIL gravity field to degree and order 310, to which a tapering function (that progressively down-weighted harmonics for degrees between ~65 and 310) was applied, such that the model has an effective half-wavelength resolution of ~70 km. Modeled crustal thickness values within Crisium vary from >25 km at the mare boundary to 2–4 km inward of the prominent ridges (Fig. 4), although in places, e.g., at Peirce crater (see Fig. 1b), the modeled crustal thickness is close to zero (Wiczeorek et al., 2013).

When viewed along two cross-sectional profiles that incorporate four of the ridges for which topography was modeled (A–A' and B–B', Fig. 1b), the subsurface geometry of each prominent fault within Crisium appears to be parallel to sub-parallel to the crust–mantle boundary beneath the basin (Figs. 4a and 4b). Along a northwest–southeast cross section, the faults under Dorsa Oppel and Harker effectively share the same dip angle as the adjacent margin of the mantle material uplifted during the formation of the basin (Fig. 4a). This same arrangement applies for the structures below Dorsa Termier and Tetyaev: they parallel the outline of the mascon to the southwest and northeast (Fig. 4b). On the basis of

these cross sections, then, Crisium's mascon appears to be structurally bounded by a set of individual faults that may have been localized by the uplifted crust–mantle boundary (see Section 6), and which define collectively a shallowly and outward-dipping reverse ring-fault system.

5. Finite-element modeling

We used the finite-element code TEKTON (Melosh and Raefsky, 1983) to test how such a structural arrangement might form under Crisium by calculating the stresses and deformation resulting from lithospheric loading within the basin. Models were configured with axisymmetric geometry, using the topographic profiles shown in Figs. 4a and 4b as the surface of the model domain and the top of the lunar crust. Far from the mare perimeter, the top of the crust was placed at a reference elevation of 0 km.

The position of the base of the crust (i.e., the crust–mantle boundary) was given largely by the calculated surface we describe above, in which the crustal thickness model of Wiczeorek et al. (2013) was subtracted from the LOLA surface topography. The models were constructed with a reference (far-field) lithosphere defined by the maximum depth, d_l , of a linear thermal gradient

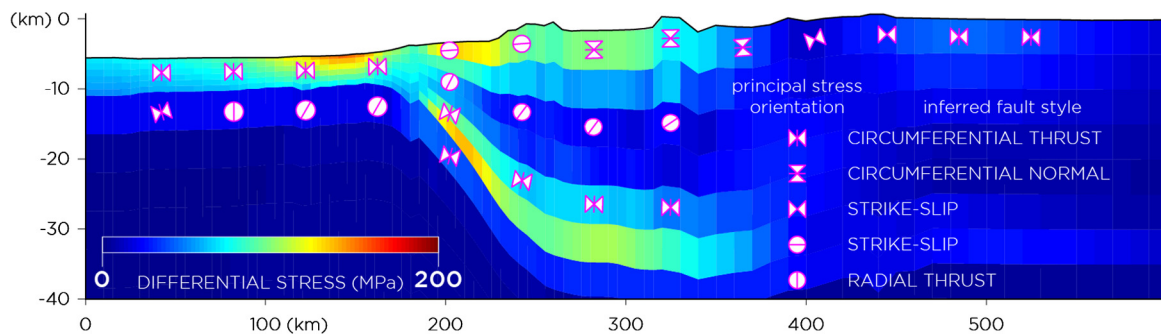


Fig. 5. Cross section of a representative, axisymmetric TEKTON model of lithospheric loading within Crisium. The symbols denote the principal stress orientations under axisymmetry (cf. McGovern and Solomon, 1993). The hourglass shapes and bars are oriented along the directions of greatest and least compressive stresses, respectively; the circles are hourglass shapes turned on their sides. The cross section is shown with a vertical exaggeration of 3.9:1.

Table 2

Parameters and values used in our TEKTON finite-element models.

Parameter	Crust	Mantle
Young's modulus, E (Pa)	6×10^{10}	1.6×10^{11}
Poisson's ratio, ν	0.25	0.25
Density, ρ (kg m^{-3})	2550	3300

below which the temperature was held constant. In our nominal models, this value was set to 30 km; we also considered d_1 values of 40, 50, and 60 km. In all cases, the far-field crustal thickness, T_c , was set to 30 km. Our models were derived with the mechanical properties of dry anorthite (Rybacki and Dresen, 2000) for the lunar crust, and those of dry olivine (Karato et al., 1986) were assigned to the lunar mantle. Key model parameters are given in Table 2; the full duration of each model run was about 73 Myr.

To ensure model stability, we limited the crust–mantle boundary relief at the center of the basin to an Airy-compensated value given by the relation $-(\rho_c/(\rho_m - \rho_c))h$, where ρ_c and ρ_m are the densities of the crust and mantle, respectively, and h is topographic elevation. This value was then multiplied by the degree of compensation, c , which we set equal to 1.75. This approach overcompensated topography in the basin interior, producing a net downward load and at least part of the mascon gravity anomaly, and underestimated the buried component of the mascon, but it allowed for a finite, numerically tractable crustal thickness. Nonetheless, the fraction of maintained crust–mantle boundary relief in each model varied from 86% to 92% of that inferred from gravity and topography. Importantly, the use of the derived crust–mantle boundary in our models correctly incorporates the basin-flanking collar of thickened crust observed at large lunar basins (e.g., Neumann et al., 1996; Andrews-Hanna, 2012) and predicted by hydrocode models (Potter et al., 2013; Miljković et al., 2014). This sub-isostatic collar produces a net upward lithospheric load.

The combination of central subsidence and flanking uplift creates the stress state shown in Fig. 5. Differential stresses in the crust form maxima at three locations: throughout the relatively thin crust near the center of the basin, and at the top and bottom of the thickened crustal collar. Stress orientations within the central stress maximum all reflect horizontal compression, with the highest stresses in this zone occurring very close to the interior edge of the topographic bench. This pattern is indicative of a uniform membrane stress state throughout the basin center associated with a component of deformation directed radially inward.

In contrast, the other two stress maxima result from a dipole stress state induced by upward flexure, characterized by horizontal extension at the top of the lithosphere and near-horizontal compression at its bottom. Notably, the orientation of the bottom stress maximum and its associated stresses follow the outward-sloping boundary that separates the central mantle plug from the flanking

crustal collar. This geometry matches well the orientation of, and sense of displacement along, the adjacent faults (Figs. 4a and 4b).

Model isotherms followed the broad variation in crust–mantle boundary depth in each setup, to approximate a post-impact thermal state of the basin, in which the thermal gradient with depth beneath the basin interior is steeper than beneath the basin exterior. Interestingly, models in which $d_1 = 40$ km showed no substantive difference from the results described above. At progressively greater values of d_1 , however (i.e., 50 or 60 km), the contribution of the mantle to lithospheric strength became ever greater, and the models failed to reproduce the fault geometries we infer from dislocation modeling.

We note that the use of the profiles in Fig. 4 to define the top of the model domain in our simulations precluded matching the modern topography. This approach, together with our model crust–mantle boundary, likely underestimated the amplitude of super-isostatic loading associating with the mascon. The magnitudes of the horizontal compressional stress within the basin have therefore been underestimated, but the spatial distribution of stresses (and thus strains) is not appreciably altered by such a scaling of mascon magnitude.

6. Synthesis

The prevalence of contractional deformation we document within Mare Crisium is consistent with earlier observations for this and other lunar maria. The penetration depths of the faults underlying the prominent, concentric wrinkle ridges is surprising, however, because thrust faults of this scale have not been reported for the Moon before. Although our method for comparing model surface displacements with topographic profiles provides a measure only of the aggregate accuracy of the entire set of model parameters, rather than of any individual parameter (e.g., fault dip), nonetheless there is a close match between the calculated geometry of these faults and the predicted orientations of stresses (and thus failure) along the stress maximum at the crust–mantle boundary in our finite-element models (Fig. 5). We therefore consider our COULOMB model results to be closely representative of the actual fault geometries present beneath Mare Crisium.

Our finite-element models indicate that the inclined crust–mantle boundary beneath the mare perimeter likely created a “flexural stress guide” that nucleated the deep-seated faults along the inner margin of the crustal collar. Models with substantial mantle contributions to the mechanical lithosphere reproduced flexural stresses that are greatest at the bottom of the lithosphere, and so failed to reproduce the stress distribution shown in Fig. 5. Since cooling of the mantle would allow it to stiffen and thus participate in the mechanical lithosphere, our results imply that the mascon-bounding faults formed early in the lithosphere's response to the basin-associated mascon and collar loads, before the

mantle had cooled substantially. Subsequent loading by mare deposits would only reinforce the stress state shown in Fig. 5, with continued or episodic faulting required to produce the topography observed within Crisium today (Fig. 1b).

In contrast to other lunar mascon maria, there is no signature of basin-concentric extension (e.g., graben) associated with Mare Crisium, deformation that is predicted by our finite-element models. The absence of graben about Crisium may be a function of a lithosphere of sufficient local thickness that loading-induced bending stresses did not exceed its tensile strength.

Wrinkle ridges within other maria (e.g., Serenitatis) continued to accumulate strain for far longer than their extensional counterparts (Solomon and Head, 1980), pointing to the later superposition of an additional source of compressional stress, e.g., from the secular cooling of the Moon's interior following an earlier period of expansion (Solomon, 1977; Andrews-Hanna et al., 2013). Therefore, although our models indicate that loading-related stresses are sufficient to produce the deformation we report, a contribution to the contractional strain observed within Crisium from global contraction cannot be discounted.

As we note above, Crisium is not the only lunar mare situated within an impact basin that has been subject to compressional stresses. It is also, however, not alone in hosting a mascon and an annular, topographic bench collocated with wrinkle ridges. For example, maria Humorum, Imbrium, Moscoviense, Nectaris, Orientale, and Serenitatis feature ridge-bounded, arcuate portions of elevated topography within their perimeters. Each of these mare deposits also has an associated mascon and so, given the spatial correlation between Crisium's prominent concentric ridges and the perimeter of the subsurface mass excess, we predict that these basins, too, are underlain by deep-seated thrusts.

Our finite-element models imply that these faults formed early, driven by annular uplift and central mantle subsidence, and do not require loading stresses from subsequently emplaced mare deposits. Conversely, deep-seated thrust faults might not form without a collar of thickened crust, and where the central positive gravity anomaly is from volcanic loading alone, as is likely the case for the mascons associated with the Argyre and Isidis basins on Mars (Smith et al., 1993). Neither Argyre nor Isidis possess an annular topographic bench, and so it may be that those basins do not host mascon-bounding, deeply rooted thrust faults. Such a scenario could also apply to Budh, Caloris, and Sobkou planitiae on Mercury, where positive free-air gravity anomalies collocate with volcanic plains (Smith et al., 2012), but where the presence of thickened crustal annuli has not been ascertained. Our results may therefore provide a framework for relating the tectonic landforms associated with a mascon basin to its subsurface structure and evolution. Given that mascons are predicted to form for most large impacts on terrestrial bodies (Dombard et al., 2013), this framework is applicable not only to lunar mascon basins, but to such impact structures throughout the Solar System.

7. Conclusions

With photogeological, topographic, and gravity data, we have explored the spatial relationship between the tectonic landforms within, and the gravity anomaly associated with, a case-study lunar mare. We find that a set of wrinkle ridges concentric to the perimeter of Mare Crisium is underlain by thrust faults that penetrate 18–20 km into the lunar lithosphere, far deeper than the base of the mare deposits themselves. These structures are collocated with the outer boundary of the Crisium free-air gravity anomaly, and in cross section appear to structurally bound the elevated crust–mantle boundary. With finite-element models, we have shown that these faults likely developed soon after impact, localized by the boundary between the subsiding superisostatic

mantle material and uplifting collar of thickened crust. The presence of wrinkle-ridge-bounded elevated terrain in other lunar mascon basins suggests that lithospheric-scale horizontal contraction, although not previously recognized for the Moon, may be integral to the mascon-forming process on that body, and perhaps on terrestrial worlds in general.

Acknowledgements

We are grateful for comments on earlier versions of this paper from two anonymous reviewers. We acknowledge support from the NASA GRAIL project, under contract NNM08AA18C to the Massachusetts Institute of Technology, and from the NASA MESSENGER project, under contract NASW-00002 to the Carnegie Institution of Washington. PJM received support from a NASA LASER Program grant (NNX13AJ60G). We thank Patrick J. Gillen for assistance with the goodness-of-fit analysis of the model fault displacement profiles. This research made use of NASA's Planetary Data System and Astrophysics Data System.

References

- Andrews-Hanna, J.C., 2012. The origin of the non-mare mascon gravity anomalies in lunar basins. *Icarus* 222, 159–168.
- Andrews-Hanna, J.C., Asmar, S.W., Head, J.W., Kiefer, W.S., Konopliv, A.S., Lemoine, F.G., Matsuyama, I., Mazarico, E., McGovern, P.J., Melosh, H.J., Neumann, G.A., Nimmo, F., Phillips, R.J., Smith, D.E., Solomon, S.C., Taylor, G.J., Wieczorek, M.A., Williams, J.G., Zuber, M.T., 2013. Ancient igneous intrusions and early expansion of the Moon revealed by GRAIL gravity gradiometry. *Science* 339, 675–678.
- Bryan, W.B., 1973. Wrinkle-ridges as deformed surface crust on ponded mare lava. In: *Proc. Lunar Sci. Conf.*, 4th, pp. 93–106.
- Byrne, P.K., Klimczak, C., Şengör, A.M.C., Solomon, S.C., Watters, T.R., Hauck II, S.A., 2014. Mercury's global contraction much greater than earlier estimates. *Nat. Geosci.* 7, 301–307.
- Chin, G., Brylow, S., Foote, M., Garvin, J., Kasper, J., Keller, K., Litvak, M., Mitrofanov, I., Paige, D., Raney, K., Robinson, M., Sanin, A., Smith, D.E., Spence, H., Spudis, P., Stern, A.S., Zuber, M.T., 2007. Lunar Reconnaissance Orbiter overview: the instrument suite and mission. *Space Sci. Rev.* 129, 391–419.
- Dombard, A.J., Hauck II, S.A., Balcorski, J.A., 2013. On the origin of mascon basins on the Moon (and beyond). *Geophys. Res. Lett.* 40, 28–32.
- Freed, A.M., Johnson, B.C., Blair, D.M., Melosh, H.J., Neumann, G.A., Phillips, R.J., Solomon, S.C., Wieczorek, M.A., Zuber, M.T., 2014. The formation of lunar mascon basins from impact to contemporary form. *J. Geophys. Res. Planets* 119, 2378–2397.
- Head, J.W., Adams, J.B., McCord, T.B., Pieters, C.M., Zisk, S.H., 1978. Regional stratigraphy and geologic history of Mare Crisium. In: Merrill, R.B., Papike, J.J. (Eds.), *Mare Crisium: The View from Luna 24*. Pergamon Press, New York, pp. 43–74.
- Hiesinger, H., van der Bogert, C.H., Reiss, D., Robinson, M.S., 2011. Crater size-frequency distribution measurements of Mare Crisium. *Lunar Planet. Sci.* 42, abstract 2179.
- Karato, S.-I., Paterson, M.S., Fitzgerald, J.D., 1986. Rheology of synthetic olivine aggregates: influence of grain size and water. *J. Geophys. Res.* 91, 8151–8176.
- Lin, J., Stein, R.S., 2004. Stress triggering in thrust and subduction earthquakes and stress interaction between the southern San Andreas and nearby thrust and strike-slip faults. *J. Geophys. Res.* 109, B02303. <http://dx.doi.org/10.1029/2003JB002607>.
- Maxwell, T.A., El-Baz, F., Ward, S.H., 1975. Distribution, morphology, and origin of ridges and arches in Mare Serenitatis. *Geol. Soc. Am. Bull.* 86, 1273–1278.
- McGovern, P.J., Solomon, S.C., 1993. State of stress, faulting, and eruption characteristics of large volcanoes on Mars. *J. Geophys. Res.* 98, 23,553–23,579.
- Melosh, H.J., Raefsky, A., 1983. Anelastic response of the Earth to a dip slip earthquake. *J. Geophys. Res.* 88, 515–526.
- Melosh, H.J., Freed, A.M., Johnson, B.C., Blair, D.M., Andrews-Hanna, J.C., Neumann, G.A., Phillips, R.J., Smith, D.E., Solomon, S.C., Wieczorek, M.A., Zuber, M.T., 2013. The origin of lunar mascon basins. *Science* 340, 1552–1555.
- Miljković, K., Wieczorek, M.A., Collins, G.S., Laneuville, M., Neumann, G.A., Melosh, H.J., Solomon, S.C., Phillips, R.J., Smith, D.E., Zuber, M.T., 2014. Asymmetric distribution of lunar impact basins caused by variations in target properties. *Science* 342, 724–726.
- Mueller, K., Golombek, M., 2004. Compressional structures on Mars. *Annu. Rev. Earth Planet. Sci.* 32, 435–464.
- Muller, P.M., Sjogren, W.L., 1968. Mascons: lunar mass concentrations. *Science* 161, 680–684.
- Mullis, A.M., 1992. An investigation of the depth of excavation and thickness of basalt fill for the lunar mascon basins. *Geophys. J. Int.* 109, 233–239.

- Neumann, G.A., Zuber, M.T., Smith, D.E., Lemoine, F.G., 1996. The lunar crust: global signature and structure of major basins. *J. Geophys. Res.* 101, 16,841–16,863.
- Okada, Y., 1992. Internal deformation due to shear and tensile faults in a half-space. *Bull. Seismol. Soc. Am.* 82, 1018–1040.
- Pike, R.J., 1977. Size-dependence in the shape of fresh impact craters on the Moon. In: Roddy, D.J., Pepin, R.O., Merrill, R.B. (Eds.), *Impact and Explosion Cratering*. Pergamon Press, New York, pp. 489–509.
- Pollard, D.D., Segall, P., 1987. Theoretical displacements and stresses near fractures in rock: with applications to faults, joints, veins, dikes, and solution surfaces. In: Atkinson, B.K. (Ed.), *Fracture Mechanics of Rock*. Academic Press, London, pp. 277–349.
- Potter, R.W., Kring, D.A., Collins, G.S., Kiefer, W.S., McGovern, P.J., 2013. Numerical modeling of the formation and structure of the Orientale impact basin. *J. Geophys. Res.* 118, 963–979.
- Rybacki, E., Dresen, G., 2000. Dislocation and diffusion creep of synthetic anorthite aggregates. *J. Geophys. Res.* 105, 26,017–26,036.
- Scholten, F., Oberst, J., Matz, K.-D., Roatsch, T., Wählisch, M., Speyerer, E.J., Robinson, M.S., 2012. GLD100: the near-global lunar 100 m raster DTM from LROC WAC stereo image data. *J. Geophys. Res.* 117, E00H17. <http://dx.doi.org/10.1029/2011JE003926>.
- Schultz, R.A., 2000. Localization of bedding plane slip and backthrust faults above blind thrust faults: keys to wrinkle ridge structure. *J. Geophys. Res.* 105, 12,035–12,052.
- Schultz, R.A., Soliva, R., Okubo, C.H., Mege, D., 2010. Fault populations. In: Watters, T.R., Schultz, R.A. (Eds.), *Planetary Tectonics*. Cambridge University Press, Cambridge, pp. 457–510.
- Smith, D.E., Lerch, F.J., Nerem, R.S., Zuber, M.T., Patel, G.B., Fricke, S.K., Lemoine, F.G., 1993. An improved gravity model for Mars: Goddard Mars Model 1. *J. Geophys. Res.* 98, 20,871–20,889.
- Smith, D.E., Zuber, M.T., Neumann, G.A., Lemoine, F.G., Mazarico, E., Torrence, M.H., McGarry, J.F., Rowlands, D.D., Head, J.W., Duxbury, T.H., Aharonson, O., Lucey, P.G., Robinson, M.S., Barnouin, O.S., Cavanaugh, J.F., Sun, X., Liiva, P., Mao, D., Smith, J.C., Bartels, A.E., 2010. Initial observations from the Lunar Orbiter Laser Altimeter (LOLA). *Geophys. Res. Lett.* 37, L18204. <http://dx.doi.org/10.1029/2010GL043751>.
- Smith, D.E., Zuber, M.T., Phillips, R.J., Solomon, S.C., Hauck II, S.A., Lemoine, F.G., Mazarico, E., Neumann, G.A., Peale, S.J., Margot, J.-L., Johnson, C.L., Torrence, M.H., Perry, M.E., Rowlands, D.D., Goossens, S., Head, J.W., Taylor, A.H., 2012. Gravity field and internal structure of Mercury from MESSENGER. *Science* 336, 214–217.
- Solomon, S.C., 1977. The relationship between crustal tectonics and internal evolution in the Moon and Mercury. *Phys. Earth Planet. Inter.* 15, 135–145.
- Solomon, S.C., Head, J.W., 1980. Lunar mascon basins: lava filling, tectonics, and evolution of the lithosphere. *Rev. Geophys. Space Sci.* 18, 107–141.
- Speyerer, E.J., Robinson, M.S., Denevi, B.W., LROC Science Team, 2011. Lunar Reconnaissance Orbiter Camera global morphological map of the Moon. *Lunar Planet. Sci.* 42, abstract 2387.
- Wieczorek, M.A., Neumann, G.A., Nimmo, F., Kiefer, W.S., Taylor, G.J., Melosh, H.J., Phillips, R.J., Solomon, S.C., Andrews-Hanna, J.C., Asmar, S.W., Konopliv, A.S., Lemoine, F.G., Smith, D.E., Watkins, M.M., Williams, J.G., Zuber, M.T., 2013. The crust of the Moon as seen by GRAIL. *Science* 339, 671–675.
- Zisk, S.H., Adams, J.B., Head, J.W., McCord, T.B., Pieters, C.M., 1978. Topographic evolution of Mare Crisium and its relation to mare filling. *Lunar Planet. Sci.* 9, 1297–1299.
- Zuber, M.T., James, P.B., 2013. Insights into lunar mare stress states from GRAIL, Abstract P13B-1753, paper presented at 2013 Fall Meeting, American Geophysical Union, San Francisco, Calif., 2013, 9–13 December.
- Zuber, M.T., Smith, D.E., Watkins, M.M., Asmar, S.W., Konopliv, A.S., Lemoine, F.G., Melosh, H.J., Neumann, G.A., Phillips, R.J., Solomon, S.C., Wieczorek, M.A., Williams, J.G., Goossens, S.J., Kruizinga, G., Mazarico, E., Park, R.S., Yuan, D.-N., 2013a. Gravity field of the Moon from the Gravity Recovery and Interior Laboratory (GRAIL) mission. *Science* 339, 668–671.
- Zuber, M.T., Smith, D.E., Lehman, D.H., Hoffman, T.L., Asmar, S.W., Watkins, M.M., 2013b. Gravity Recovery and Interior Laboratory (GRAIL): mapping the lunar interior from crust to core. *Space Sci. Rev.* 178, 3–24.